Nanoscale

ROYAL SOCIETY
OF **CHEMISTRY**

PAPER
Yasin B. Seven *et al.*
Rapid mapping of spinal and supraspinal connectome *via*
self-targeting glucose-based carbon dots

NCNST

PAPER

View Article Online
View Journal | View Issue

Rapid mapping of spinal and supraspinal connectome *via* self-targeting glucose-based carbon dots

Yasin B. Seven, [iD] *[a,b,c] Elif S. Seven, [iD] [d,e] Emel Kirbas Cilingir, [iD] [d] Komal Parikh,[f] Mehmet Aydin, [iD] [a] Edward K. Luca,[f] Jayakrishnan Nair[g] and Roger M. Leblanc [iD] [d]

The spinal cord is a highly dynamic network, playing significant roles in the vital functions of the brain. Disorders of the spinal cord, such as spinal cord injury and amyotrophic lateral sclerosis (ALS), are associated with neurodegeneration, often resulting in morbidity and mortality. The blood-brain barrier (BBB) poses a major challenge to imaging and therapeutic agents because less than 2% of small-molecule drugs and almost no large-molecule drugs can cross the BBB. Furthermore, spatial spectroscopy studies have shown highly heterogeneous BBB crossing with significant accumulation at the unintended brain regions. Thus, targeting systems that can cross the BBB at the spinal cord and precisely target specific cell types/populations are vitally needed. Carbon dots can be custom-designed to accumulate at the spinal cord; thus, they offer great potential as delivery platforms for imaging and therapeutic approaches. Since neurons are metabolically highly active and rely on glucose, we designed glucose-based carbon dots (GluCDs) with a diameter of ~4 nm and glucose-like surface groups. We determined the CNS distribution of GluCDs on three scales: 1. brain regional distribution, 2. cellular tropism (*e.g.* neurons *vs.* glia), and 3. intracellular localization. We found that GluCDs (1) crossed the BBB at the spinal cord level, localized primarily to the spinal cord, and were quickly transported to higher centers in the brain, revealing supraspinal connectome within 4 hours after systemic delivery (minimally invasive and significantly faster than the available technologies); (2) almost exclusively localized to neurons without the need for a targeting ligand (neuronal self-targeting), and (3) were confined to late endosomal/lysosomal compartments in the neurons. Then, we verified our findings in a cervical spinal cord contusion injury model with GluCDs targeting the neurons at the injury epicenter. Therefore, GluCDs can be used as robust imaging agents to obtain rapid snapshots of the spinal/supraspinal network. GluCD nanoconjugates can open new avenues for targeted imaging of spinal cord injury. These findings can be extended to other spinal disorders such as ALS, spinal muscular atrophy, and spinal stroke.

Introduction

Delivery of imaging and therapeutic agents across the blood-brain barrier (BBB) is a formidable problem, limiting the development of effective neuroimaging and neurotherapeutic agents.[1–3] The BBB represents a major obstacle because less

[a]Dept. of Physiological Sciences, University of Florida, Gainesville, FL, 32603, USA. E-mail: yasinbseven@ufl.edu
[b]Breathing Research and Therapeutics (BREATHE) Center, University of Florida, Gainesville, FL
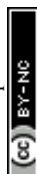*[c]McKnight Brain Institute, University of Florida, Gainesville, FL, 32610, USA*
[d]Department of Chemistry, University of Miami, Coral Gables, FL, 33146, USA
[e]C-Dots Nanotec LLC, Gainesville, FL, 32601, USA
[f]Dept. of Physical Therapy, University of Florida, Gainesville, FL, 32603, USA
[g]Dept. of Physical Therapy, Thomas Jefferson University, PA, 19107, USA

than 2% of small-molecule drugs and almost no large-molecule drugs can cross the BBB.[4,5] Notably, even small molecules that can cross the BBB achieve much lower concentrations in the brain than the plasma.[6,7] Furthermore, according to spatial spectroscopy studies, these molecules show highly heterogeneous BBB crossing with significant targeting at the unintended brain regions or cell types/populations.[7] Thus, delivery systems that can cross the BBB at the desired brain regions and precisely target specific cell populations are vitally needed.

The spinal cord plays a significant role in the communication, data processing, and coordination between the brain and the peripheral nervous system. Motor functions, such as breathing and locomotion, and sensory functions, such as pain and touch, rely on adequately functioning spinal circuits.[8–12] Spinal cord disorders such as spinal cord injury (SCI), spinal stroke in aortic surgery, amyotrophic later scler-

osis (ALS), spinal muscular atrophy (SMA), Friedreich's ataxia, and multiple sclerosis are often associated with neuronal loss and highly dynamic reorganization of spinal and supraspinal networks.[13–16] Despite the prevalence and severity of these conditions, *there is no rapid and minimally invasive small molecule delivery system selectively targeting the spinal neurons and associated circuits.*

Carbon dots are spherical carbon-based nanoparticles with tunable physicochemical and optical properties.[17–19] Precursors and synthetic methods significantly affect the properties of the carbon dot and their interactions with the biological environment,[20] leading to differences in tissue distribution and biological interactions. Thus, carbon dots represent highly customizable nanoplatforms that can be conjugated with fluorophores, small molecule drugs, and siRNAs for imaging and therapeutic purposes.[21–23] Neurons are metabolically highly active and rely primarily on glucose as their energy source. To leverage the high glucose demand that neurons

require to deliver imaging agents, we recently characterized ultrasmall, amphiphilic glucose-based carbon dots (GluCDs) of approximately 4 nm in diameter that crossed the BBB *in vivo* and showed no measurable cytotoxicity in healthy cell lines.[20,24,25] However, the distribution and behavior of GluCDs in the central nervous system (CNS) were not described.

In this study, we determined the CNS distribution of GluCDs on three scales: 1. regional distribution (*e.g.* spinal cord, cerebellum, and motor cortex), 2. cellular specificity/tropism (*e.g.* neurons and astrocytes), and 3. intracellular localization (cytoplasmic or a specific organelle). We showed that GluCDs 1. effectively cross the BBB selectively at the spinal cord level, carrying small-molecule cargo, and were quickly transported to higher centers in the brain *revealing spinal cord connectome faster than available technologies*, 2. almost exclusively localize to neurons without the need for a targeting ligand, and 3. localize to late endosomes/lysosomes. In addition, we tested GluCDs in a cervical SCI model and
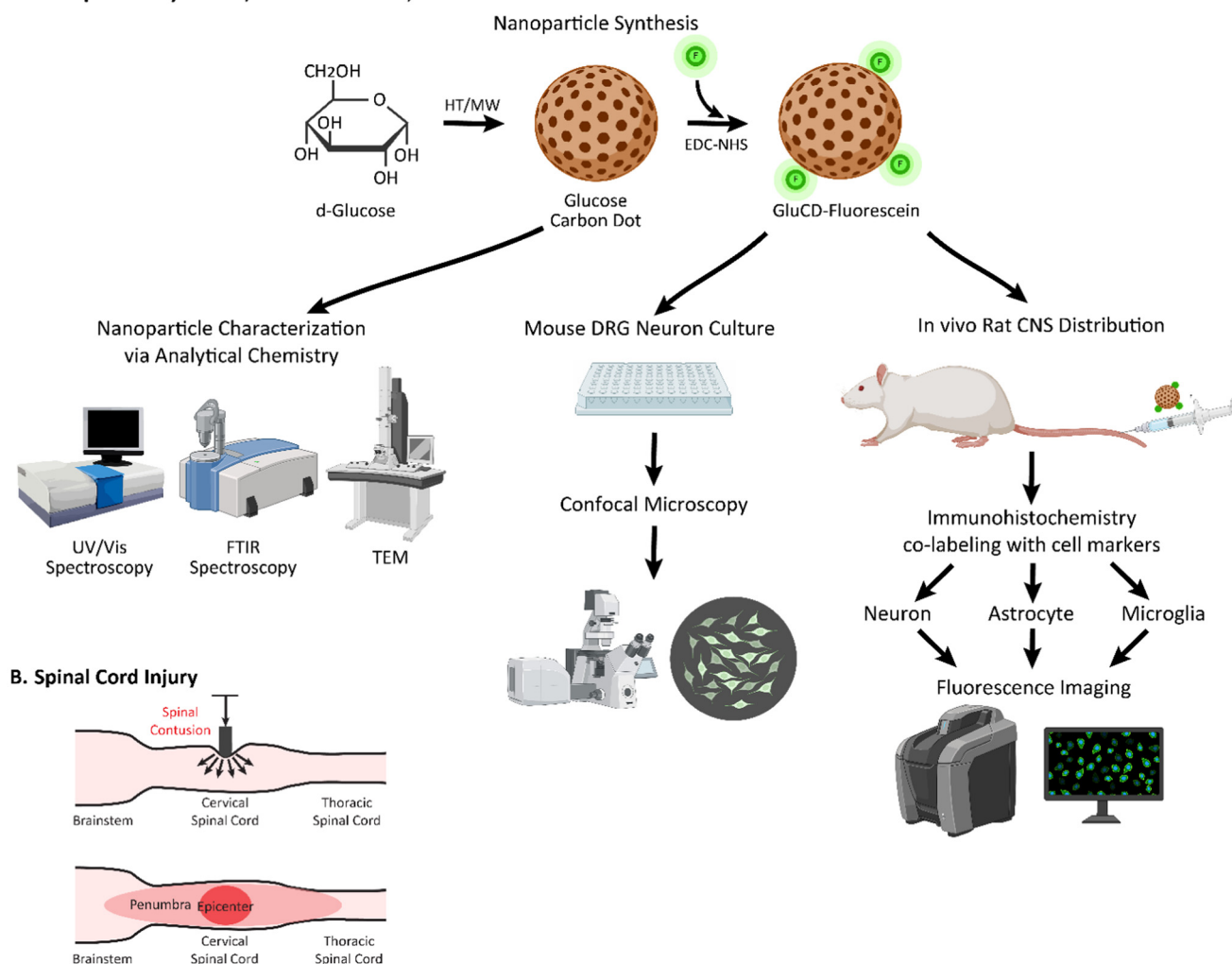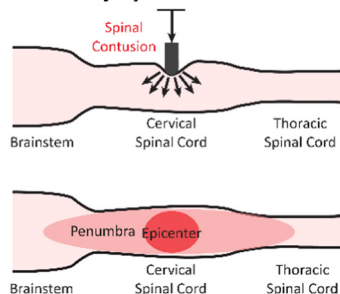

Fig. 1 Summary of methods: (A) flowchart of the methods for GluCD characterization and *in vitro* and *in vivo* studies. GluCDs were used for *in vitro* studies and GluCD-F was used for *in vivo* studies. Fluorescence imaging was performed *via* epifluorescence and super-resolution confocal microscopies. (B) Spinal cord contusion performed at the C4 level. Created in BioRender. Seven, Y. (2025) https://BioRender.com/su9fj9l.

observed that GluCDs penetrate to the injury epicenter and target neurons when administered intravenously after cervical SCI. Our findings indicate that GluCD nanoconjugates can open new avenues for targeted imaging and treatment of SCI. These findings can be extended to other spinal disorders, such as ALS, SMA, and spinal stroke.

Results and discussion

Glucose carbon dot characterization

Following synthesis and purification, GluCDs were lyophilized to obtain a dry powder. The physical appearance of GluCDs after lyophilization was brownish. The GluCD yield was approximately 0.4% per initial D-glucose weight. To evaluate the utility of GluCDs beyond the initial synthesis, we next assessed their long-term stability. We observed comparable fluorescence intensities and central nervous system distribution for freshly prepared (Fig. S3) and 2-year-old batches,[20] indicating their high stability. Furthermore, the photoluminescence intensity of GluCDs remained stable and did not quench after repeated imaging using fluorescence or confocal microscopy. The PL of GluCDs was excitation-dependent, whereas the PL of GluCD-F was excitation-independent (Fig. S3), which is consistent with our previous work.[25] We conducted additional characterization of the CDs as a quality control measure to confirm the batch-to-batch consistency of the synthesis (Fig. 1).[20,24,25]

In our earlier studies, we extensively characterized GluCDs and their conjugates by UV/vis, PL, FTIR-ATR, XPS and Raman spectroscopy, TGA, TEM and AFM.[20,24,25] Fig. 2A shows a representative TEM image showing the round-shaped GluCDs. The diameters of GluCDs used in the studies were within the range of 3 to 8 nm.[20] GluCDs were covalently conjugated to fluorescein (GluCD-F), and was characterized previously[20,25] to test their cargo loading and enhance the fluorescence intensity.[20,24,25] The Fourier-transform infrared (FTIR) spectrum of GluCDs is shown in Fig. 2B. The wide prominent peak centered around 3335 cm^{-1} is consistent with hydroxyl groups (–OH stretch) in all samples. The sharp peak at 1020 cm^{-1} is mainly due to C–O stretching of the C–O–C and C–O–H bonds. The peaks at 1703 nm and 1610 nm correspond to C=O and C=C bonds, respectively. The UV/vis spectrum (Fig. 2C) shows two bands between 200 nm and 300 nm, suggesting a π–π* transition, likely due to aromatic ring formation.[20]

Glucose carbon dots target spinal neurons with high specificity and localize to the late-endosomal/lysosomal compartment

After GluCD-F administration *via* tail injections, initial observations suggested the presence of GluCD-F throughout the spinal cord, likely due to the higher permeability of the BBB at the spinal cord level.[26–28] In contrast, only a few locations were targeted in the higher brain centers. In imaging studies, the fluorescence intensity was minimal at the cervical spinal cord 45 minutes after intravenous delivery. However, four hours
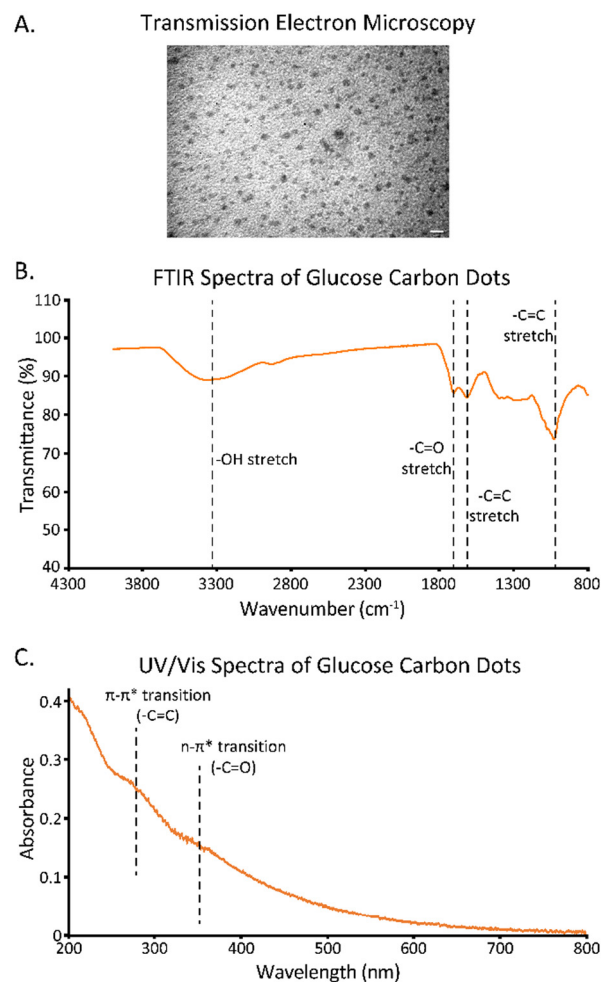

Fig. 2 Characterization of glucose carbon dots: (A) representative transmission electron microscopy image (Scale bar: 10 nm) and (B) FTIR- (C) and UV/Vis spectra.

after delivery, significant green fluorescence was observed in the grey matter, which remained for at least 5 days (the longest time point recorded).

Next, GluCD-F was co-immunolabelled with a neuronal marker (NeuN), astrocytic marker (GFAP), or microglial marker (IBA1) to study the cellular specificity. Fig. 3A and B show that GluCD-F is almost exclusively colocalized with NeuN + neurons and distributed in a granular fashion in the perinuclear compartment of the cytoplasm. Thus, once internalized at the cell membrane, GluCDs are retrogradely carried to the perinuclear region. When we quantified the ratio of fluorescein fluorescence in cell marker-labelled regions to the fluorescence in the entire image, approximately 94.5% of the total fluorescence was observed within the NeuN + areas, displaying strong neurotropism (Fig. 3C). We observed that NeuN labels neuronal nuclei and somata, but not distal dendrites and axons, indicating that this number is conservative. Astrocytes did not contain detectable amounts of GluCDs, whereas microglia contained <5% of GluCDs. To support the colocalization analyses, we plotted the two-dimensional Pearson's correlation
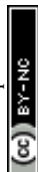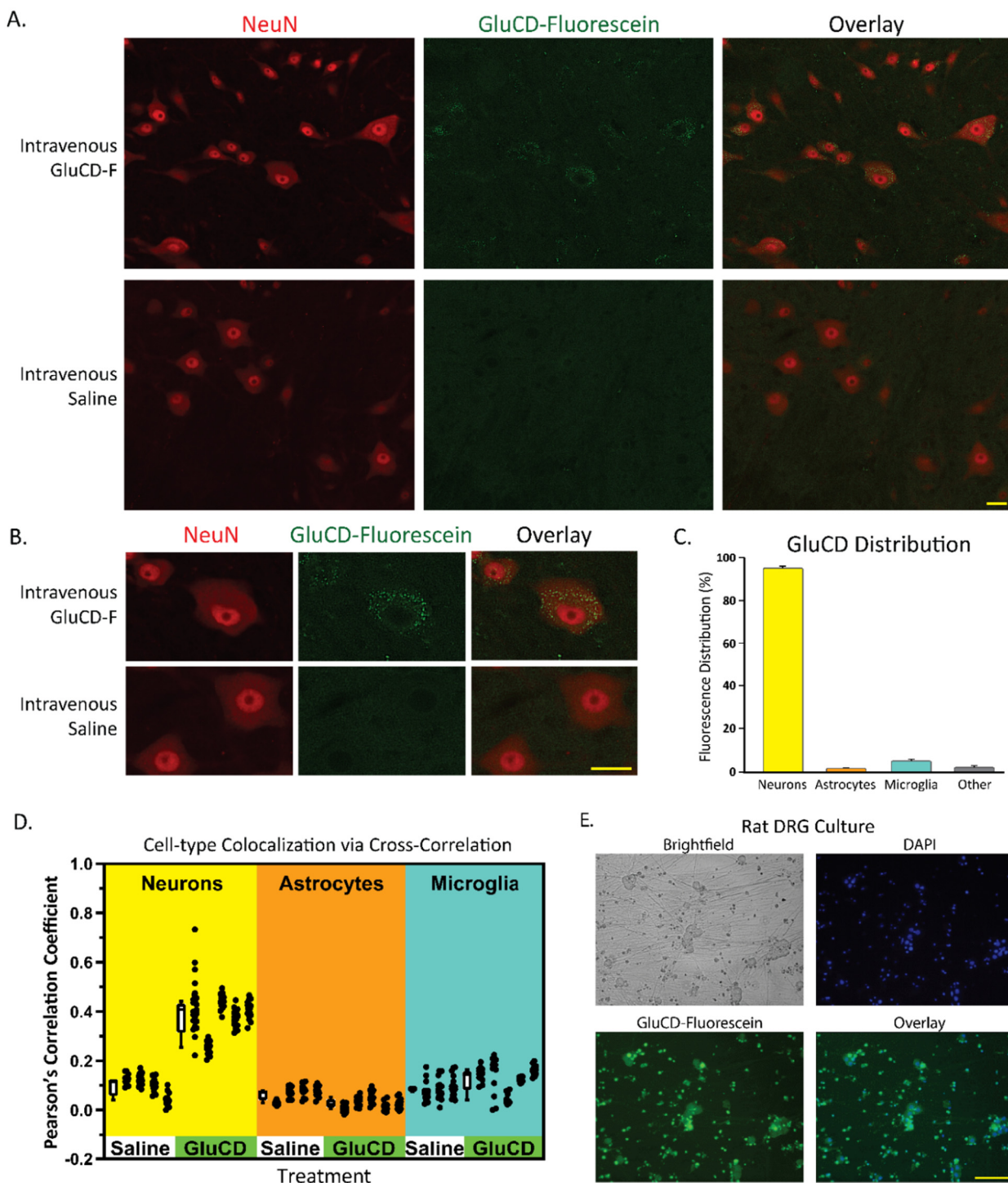
Fig. 3 Neuronal colocalization of glucose carbon dot-fluorescein (GluCD-F) conjugates in the cervical spinal cord following intravenous delivery. (A) Representative histological sections following GluCD-F (top panels) or saline (bottom panels) administration. In the left panels, neurons are labelled with NeuN (red). Middle panels show GluCD-F localization (green). The right panels show the colocalization *via* the overlay. GluCD-F colocalize with neurons. Scale bar: 25 μm. (B) Zoomed-in view showing the neuronal colocalization and the granular distribution of GluCD-F. Scale bar: 25 μm. (C) Approximately 95% of the observed fluorescence is localized within neurons, whereas ~4% is localized within microglia. (D) Pearson's cross-correlation coefficients between red and green channels are shown for each image to determine the cell type distribution. The localization of GluCD-F correlates with neuronal marker, but not other cell type markers. (E) Histological visualization of GluCD-F treatment in rat DRG neuron cultures. The first figure is a brightfield overview. Nuclei are shown by DAPI (blue). Green fluorescence shows the GluCD-F uptake. Scale bar: 100 μm.
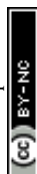
coefficient between each cell marker with GluCDs (Fig. 3D). GluCD-treated astrocytes and microglia were not significantly different from saline controls (0–15%). In contrast, neurons showed a significant correlation with GluCD (~40%). GluCDs localize to nearly all neurons in the cervical spinal cord rather than a subset. Two observers counted 98.3% of NeuN + neurons contained GluCD with a range of 95.9–100% per spinal cord section. Overall, GluCDs effectively crossed the blood-spinal cord barrier and localized extensively in spinal neurons rather than glia (Fig. 3, Fig. S1). Neuroimmune response is a major concern for viral targeting methods[29] because non-functionalized nanomaterials crossing the BBB are frequently scavenged by macrophages and microglia.[30–33] Hence, nanomaterials that can escape the microglia are crucial for targeting other cell types in the CNS, such as neurons. Here, we leveraged the high glucose demand of neurons to deliver GluCDs with glucose-like surface groups, suggesting self-targeting property.[25] Furthermore, microglia do not show a proinflammatory phenotype, which suggests a favourable biocompatibility. Lastly, we generated rat dorsal root ganglion (DRG) cultures to verify that the GluCDs can target neurons outside the BBB. Fig. 3E shows that rat DRG neurons are positive for GluCDs.

To determine the intracellular localization, we performed LAMP1 immunohistochemistry. LAMP1 is a late endosomal and lysosomal marker. Fig. 4 shows the nearly complete overlap between GluCDs and LAMP1, suggesting that GluCDs localize to late endosomes and lysosomes. Of particular note, GluCDs are distributed homogeneously in the perinuclear

compartment, with some polarized clustering of lysosomes (Fig. 4A and B, Fig. S2). Finally, we also confirmed the intracellular GluCD distribution *via* 3D super-resolution confocal microscopy (see the SI video). These results suggest that GluCDs can be used to image neuronal lysosomes, which can be invaluable for studying spatial lysosomal dynamics.

Glucose carbon dots reveal supraspinal connectome within 4 hours; significantly faster than previously established techniques

GluCD localization studies in the medulla, midbrain, cerebrum, and cerebellum showed that GluCD localization is not as extensive as in the spinal cord and does not follow a diffuse pattern when present. Often, GluCDs target a particular band or a focal area of neurons but not the adjacent centers. Furthermore, GluCDs are localized in neurons at specific brain centers, mostly with direct connections to the spinal cord. The primary areas of GluCD targeting were the areas associated with premotor neurons in the medulla, thalamus, lamina/layer V at the cerebral cortex, and some olfactory areas such as the piriform cortex.[13] Fig. 5 shows the lamina V and thalamus labelling, which is not a diffuse pattern but a select group of cells. These connections are likely direct sensory or motor connections to the spinal cord. In addition, some neurons indirectly connected to the spinal cord, such as Purkinje neurons, were also GluCD+, suggesting the possibility that GluCDs cross the synapses to higher order neurons.

GluCD targeting occurs within at most 4 hours after intravenous administration and lasts up to 5 days (maximum timespan that the experiments were conducted). In comparison, commonly used retrograde labelling methods often require 2–14 days. Some examples of these traces are fluorogold (3–13 days[34–37]), fast blue (3–14 days[38–41]), cholera toxin beta subunit (2–3 days[42,43]), wheat germ agglutinin (2–3 days[44–47]), and pseudo-rabies virus (24–48 hours[48–53]). More recent methods of AAV-mediated retrograde labelling are invasive and require 7–14 days. A recent elegant study of AAV-mediated supraspinal connectome tracing needed 2–4 weeks post-spinal injection.[13] We observed significant overlap between the brain regions labelled by intraspinal AAV injections of Wang *et al.* and our rapid minimally invasive (intravenous) method. Thus, the GluCD method offers a minimally invasive approach that provides a snapshot of supraspinal connectivity faster than the current methods. This method can be useful for elucidating the highly dynamic neural architecture of the spinal and supraspinal pathways during normal function and disease.[13]

Glucose carbon dots penetrate to the injury epicenter and maintain neurotropism after cervical spinal cord contusion injury

An important problem involving the spinal cord is SCI. Cervical SCI is very commonly observed in vehicle accidents, where the blood supply to the spinal cord is impaired *via* acute hypotension and disruption to the local microvasculature, followed by coagulation. Thus, blood flow is most impaired in the areas where therapeutics are needed the most.
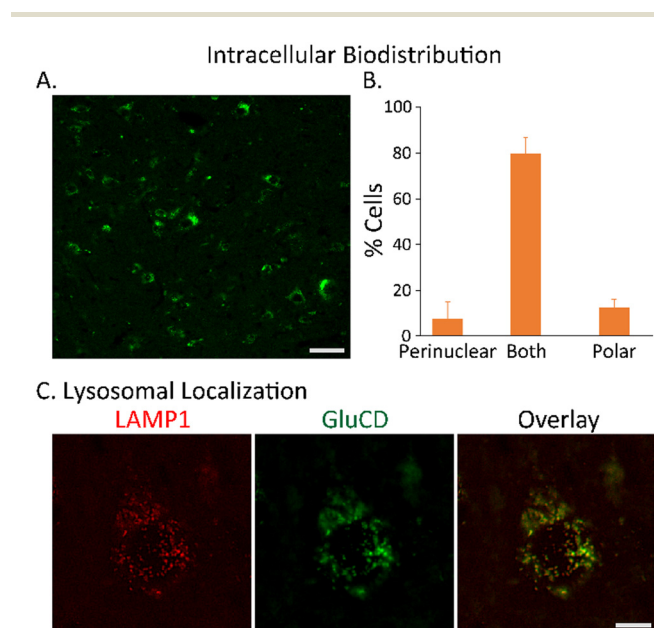

Fig. 4 Intracellular distribution of glucose-based carbon dots (GluCDs). (A) Cervical spinal distribution of GluCDs showing neuronal features. (B) Perinuclear symmetric distribution with polarization is the most common intracellular distribution. (C) GluCDs colocalized with LAMP1-positive intracellular vesicles, *i.e.*, late endosomes/lysosomes. Scale bars: 50 μm (A) and 10 μm (C).
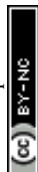
A. Cortex: Lamina V
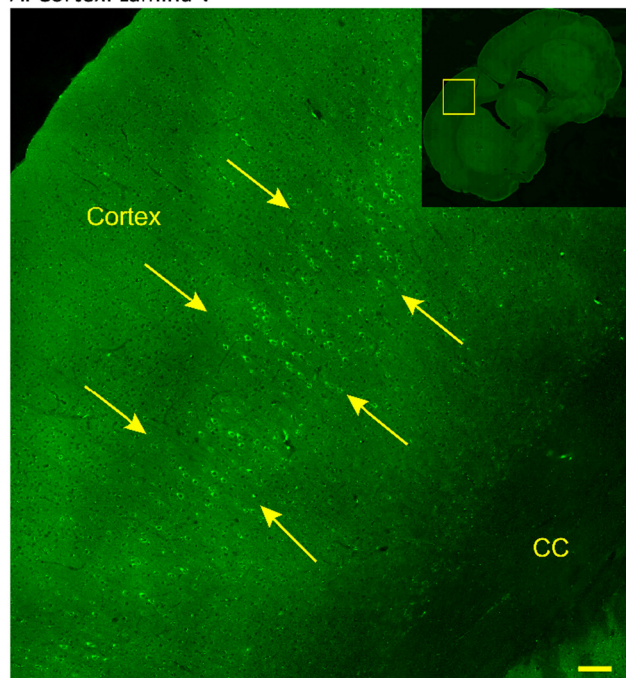
B. Cerebellum: Purkinje Cells
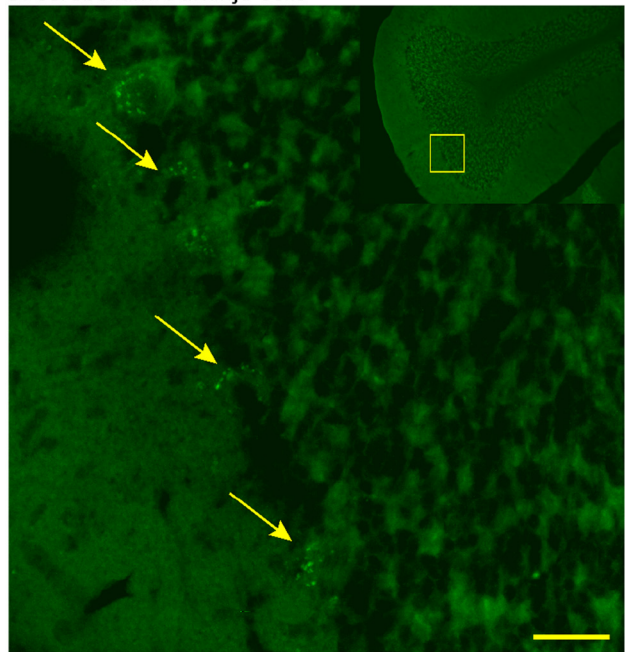

Fig. 5 Representative images of glucose carbon dots targeting the supraspinal network. (A) Cortex: Layer V neurons are selectively positive for GluCDs. Other layers are devoid of GluCDs (green). (B) Purkinje cells in the cerebellum are GluCD-positive. Scale bars: 100 μm (A) and 30 μm (B).

To determine the targeting efficacy of GluCDs to the epicenter of the SCI, we performed mid-cervical spinal contusion at the C3/4 segment and administered GluCDs after 3 hours, which is much longer than expected for coagulation to take place. Four hours after administration, we determined the biodistri-
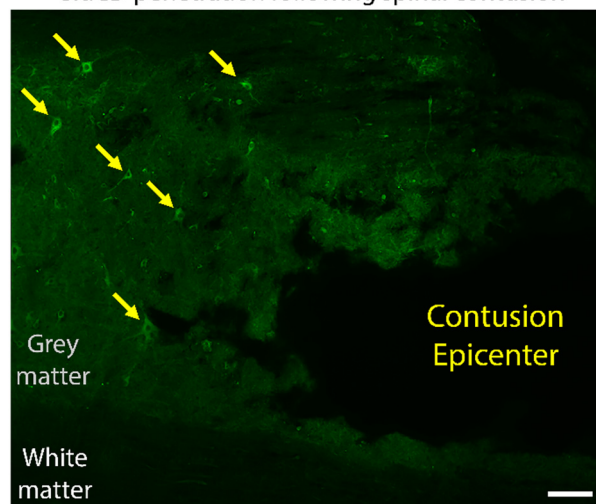
GluCD penetration following spinal contusion

Fig. 6 Representative image of a longitudinal section of cervical spinal cord with glucose carbon dot (GluCD) treatment after mid-cervical spinal contusion injury. Neuronal somata (grey matter) are GluCD-positive. Scale bar = 200 μm.

bution of GluCDs in the spinal cord. Similar to intact animals, GluCDs were present in neurons after injury (Fig. 6). Neuronal fluorescence intensities were stronger in the soma and dendrites at the injury epicenter, suggesting that neuronal GluCD uptake is enhanced with acute SCI.

Conclusion

The BBB and innate immune responses are major obstacles for the delivery of imaging agents and therapeutics for various neurological disorders. Therefore, it is crucial to develop minimally invasive and less immunogenic delivery platforms that can effectively and robustly cross the BBB and reach the CNS. Here, we report that glucose-based carbon dots can cross the BBB selectively in the spinal cord, likely due to increased permeability of the BBB at the spinal cord[26–28] (Fig. 7A and B). Furthermore, GluCDs localize to spinal neurons with high specificity (Fig. 7). The GluCDs then retrogradely target the supraspinal network following the spinal route (Fig. 7B); the process is faster than currently available techniques. Intracellularly, neuronal lysosomes appear to be the target organelle (Fig. 7C). Importantly, GluCDs effectively penetrated into the spinal contusion injury epicenter. Thus, GluCDs may be effective imaging and therapeutic delivery tools for neurological disorders of the spinal cord.

Experimental

Materials and instrumentation

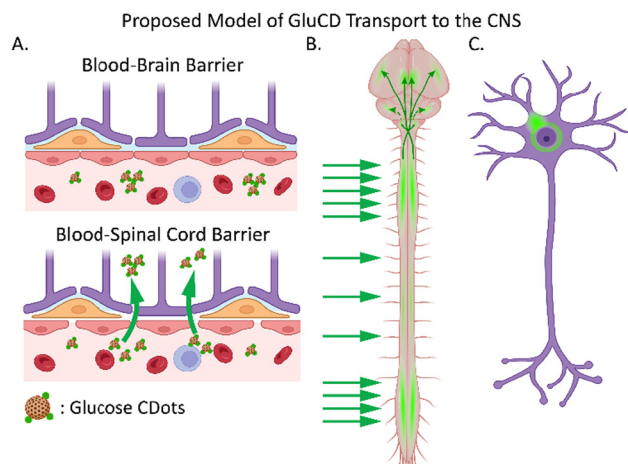D-Glucose and NaOH pellets (98.5%) (nitrogen flushed, hygroscopic) were purchased from VWR International, LLC (Radnor,

Fig. 7 Proposed model of glucose carbon dot (GluCD) transport to the central nervous system (CNS). (A) GluCDs cross the CNS barrier at the spinal cord level. (B) GluCDs are carried to higher centers, targeting the supraspinal connectome. (C) GluCDs are neurotropic with late endosomal/lysosomal localization. Created in BioRender. Seven, Y. (2025) https://BioRender.com/9lw7o8s.

PA) and Acros Organics, respectively. DI–H_2O with a resistivity of 18 MΩ cm at 20.0 ± 0.5 °C and surface tension of 71.2 mN m^{-1} was used for all reactions and purification steps (Direct-Q 3 water purification system; EMD Millipore Corp.; Chicago, IL). Pre-treated Spectra/Por 7 dialysis membrane tubing (1 kDa MWCO, Spectrum Laboratories Supply, Inc., Rancho Dominguez, CA) and syringe filters (0.2 μm, VWR, Radnor, PA) were used for GluCD purification. The samples were lyophilized using a FreeZone 4.5 L cascade benchtop freeze-dry system (Labconco, Kansas City, MO). All aqueous CD samples were sonicated prior to characterization using a Branson 1510 ultrasonicator (Gaithersburg, MD). All chemicals were used as received without further purification.

Carbon dot preparation

GluCDs were prepared using a bottom-up approach with glucose as the sole precursor *via* our previously published hydrothermal carbonization method.[20,24,25] Hydrothermal carbonization was performed in a Teflon-coated autoclave reactor with glucose dissolved in ultrapure water at a final concentration of 10% w/w. The reaction temperature was set to 200 °C for a duration of 5 h. After the reaction, the contents of the reactor were transferred to a centrifuge tube and centrifuged at 3000 rpm, at 4 °C for 20 min. The supernatant was syringe-filtered to remove the leftover precipitation. The filtered solution was neutralized using a super-saturated NaOH solution. Finally, the sample was lyophilized to yield a solid product. GluCD-F conjugates were prepared with EDC-NHS ester conjugation using our previously published method.[25]

Characterization of carbon dots

UV/vis absorption spectra of the CDs dispersed in DI–H_2O were acquired using a Cary 100 UV/vis spectrophotometer

(Agilent Technologies, Inc.; Santa Clara, CA, USA) and a semi-micro-quartz cuvette with 1 cm path length and two dark walls (Starna Cells, Inc). Photoluminescence (PL) emission spectra were obtained with a Horiba Jobin Yvon Fluorolog-3 (Horiba, Ltd; Piscataway, NJ, USA) with a slit width of 5 nm for both excitation and emission. A quartz cuvette with all clear walls and a 1 cm path length (Starna Cells, Inc) was used for the PL emission measurements. Data analysis and plotting were performed using ORIGIN Software (OriginLab Corp., Northampton, MA). A Fourier-transform infrared spectrometer equipped with attenuated total reflection accessories (FTIR-ATR, Perkin Elmer, Inc.; Waltham, MA, USA) was used to acquire FTIR spectra of lyophilized CDs with air as background.

A JEOL 1200× transmission electron microscope (TEM) was used for morphological studies using a carbon-coated copper grid. A drop of the aqueous CDs solution was placed on the grid and air-dried before imaging.

Rat dorsal root ganglion cultures

Rat dorsal root ganglion (DRG) neuron cultures for bioimaging studies were generously provided by Yelena Pressman at the University of Miami. DRG neurons were isolated from the dorsal root ganglia of embryonic rats (E15) according to an established protocol.[54] DRG neurons were plated on poly-L-lysine/laminin-coated 24-well (Corning, NY, USA) plates in neurobasal media supplemented with B-27, L-glutamine and nerve growth factor (Gibco). Cultures were treated with 10 μM fluoro-deoxyuridine to prevent contamination. First, to confirm the viability of the neurons in the culture, immunocytochemistry was performed for neurofilament and β-Tubulin. One week after isolation, the neurons were treated with 500 μM GluCD-Fluorescein for 24 hours, washed with PBS, and pre-fixed with a couple of drops of fresh 4% paraformaldehyde (PFA) for 5 minutes. PBS and PFA were aspirated gently, and neurons were post-fixed with fresh 4% PFA for 10 minutes, followed by a PBS wash (2×). After fixation, the DRGs were blocked with 5% bovine serum albumin (BSA) with 0.6% Triton-X100. Primary antibodies targeting neurofilament (Thermo Fisher Scientific, Waltham, MA) and β-tubulin (Cell Signaling, Danvers, MA) were applied. For negative controls, the neurons were incubated with antibody diluent only (2.5% BSA, 0.3% Triton-X100 in PBS). Secondary antibodies, Alexa Fluor 594 goat anti-mouse and Alexa Fluor 488 goat anti-rabbit (Thermo Fisher Scientific, Waltham, MA), were then applied. One drop of antifade reagent with DAPI was added and a cover slip was inserted carefully on top of each well before imaging with an EVOS Floid Cell Fluorescence Microscope.

Animals

Animal experiments were approved by the Institutional Animal Care and Use Committee at the University of Florida in accordance with the National Institutes of Health Guide and Use of Laboratory Animals. 19 adult male Sprague-Dawley rats were studied (~350–400 g, Harlan, Indianapolis IN, Colony 208A). Rats were maintained on a 12 h light/dark cycle with access to food and water *ad libitum*.
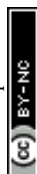
Intravenous injections

Anesthesia was induced in a gas chamber (2.5% isoflurane in O_2) and maintained *via* a nose cone (2% isoflurane in O_2) on a surgical heating pad. Intravenous (IV) injections were performed at the lateral tail vein as described earlier.[55,56] The tail vein was catheterized (24 Gauge; Surflash, Somerset, NJ) and administered with GluCD-F conjugate in sterile saline (0.9% NaCl) or vehicle. The total dose of GluCD-F was 10 mg kg^{-1} at 2 mg mL^{-1} (mass/volume). The intravenous catheter was then removed, and the injection site was pressurized until bleeding stopped. Rats were kept awake for 45 min (imaging), 4 h (imaging) or 7 days (imaging and toxicity, Fig. S4). In addition to cellular toxicity analyses,[20] no abnormal signs of stress were observed *in vivo*. Weight gains were normal for 7 days after GluCD delivery and microglia were not activated.

C4 spinal contusion

Anesthetic and surgical preparation methods were described previously.[57–60] First, anesthesia was induced in a gas chamber (3% isoflurane in O_2) and maintained *via* a nose cone (2–2.5% isoflurane in O_2) during surgery. The adequacy of anesthesia was verified by the absence of toe pinch reflex. A heating pad was used to maintain body temperature. Artificial tears were applied, and nails were clipped. Meloxicam (2 mg kg^{-1}) was administered subcutaneously to minimize inflammation. The surgical area was shaved and cleaned with betadine.

Following a cervical incision from the base of the skull to the C6 segment, C4 spinal cord was exposed *via* laminectomy while keeping the dura intact. A midline contusion was performed using the Infinite Horizons Impactor (Precision Systems and Instrumentation, LLC, Lexington, KY) after the spine was stabilized *via* 2 forceps near C3 and C5 levels.[61–64] A 1.3 mm-diameter tip was used to deliver 125 kdyn force with 0 s dwell time. Probe force and displacement were measured in real-time to ensure no accidental bone impacts occurred. Following contusion, muscles were sutured, and skin was closed with wound clips. Sterile lactated Ringer's solution (5 mL) was administered subcutaneously for fluid loss due to surgery. Nanoconjugates were delivered by IV, 3 hours after injury. Rats were sacrificed at 7 h post-injury for further analyses.

Histology and immunolabeling

All rats were perfused transcardially with 0.01 M PBS (4 °C, pH 7.4) followed by 4% paraformaldehyde (PFA) in 0.01 M PBS (4 °C, pH 7.4) at the terminal time points. Brain and spinal cord were harvested, fixed in 4% PFA (4 °C, pH 7.4) overnight, and cryoprotected in 20% followed by 30% sucrose solution (4 °C). Harvested tissues were protected from light where possible. All tissues were sectioned in the transverse plane using a freezing microtome (40-μm thickness; SM2010R, Leica; Buffalo Grove, IL). Sectioned tissue slices were stored in antifreeze solution (30% glycerol + 30% ethylene glycol + 40% 0.1 M PBS) at −20 °C. More than 6 cervical spinal samples and 8 medulla samples were uniformly selected for histological analyses.[60]

Immunohistochemistry was performed to label different cell types in the cervical spinal cord. Each cell marker protein was immunolabeled in a single batch to reduce batch-to-batch variability. Tissues were triple-washed in PBS (0.1 M, pH 7.4) and incubated with 5% normal donkey serum (NDS), 0.1% bovine serum albumin, and 0.1% Triton X-100 in 0.1 M PBS (PBS-Tx) for 1 h. The tissues were then incubated with one of the following: (1) mouse anti-NeuN (Neurons, 1 : 500; catalog no: MAB377, Millipore Sigma), (2) rabbit anti-GFAP (Astrocytes, 1 : 1000, catalog no: AB5804, Millipore), (3) mouse anti-IBA1 (Microglia, 1 : 500, catalog no: MABN92, Millipore), or (4) rabbit anti-LAMP1 (Late endosomes/lysosomes, 1 : 250, catalog no: 9091, Cell Signalling) primary antibodies in 2.5% NDS with PBS-Tx at 4 °C for 2 overnights. Tissues were triple-washed in PBS and incubated in donkey anti-mouse or donkey anti-rabbit (594, 1 : 500, Thermofisher) secondary antibodies, 2.5% NDS, and PBS-Tx at room temperature for 2 h. After the final wash, tissue sections were mounted on charged slides (Fisher) with hard-set anti-fade medium (Vector Labs) and cover-slipped. On a separate set of control tissues, no immunohistochemistry was performed to confirm that the nanoconjugate distributions in immunohistochemistry-treated and untreated tissues were the same.

Image acquisition and analysis

Tissue sections were imaged *via* epifluorescence and super-resolution confocal microscopies. First, imaging was performed using an epifluorescence microscope with a 20× PlanApo lens (Keyence BZ-X700, Keyence Corporation of America, Itasca, IL). GluCD-Fluorescein conjugate was imaged at excitation and emission wavelengths of 470/40 nm and 525/50 nm (GFP filter: OP-87763). Cell markers were imaged at the excitation and emission wavelengths of 560/40 nm and 630/75 nm (Texas red filter: OP-87765). For each image set (*e.g.*, Neuronal marker + GluCD-Fluorescein), the image acquisition settings were used for both vehicle and treatment groups. We determined nanoconjugate colocalization using three methods: (1) % colocalization: determining the total nanoconjugate fluorescence intensity within a cell type divided by the overall total nanoconjugate fluorescence intensity, (2) pixel-to-pixel 2-dimensional cross-correlation between nanoconjugate fluorescence intensity and cell marker intensity with MATLAB, and (3) cell-by-cell classification of nanoconjugate positive/negative cells by 2 independent operators. We confirmed our intracellular localization and distribution findings using a Nikon CSU-W1 SoRa super-resolution confocal microscope (112×, 40× lens, 2.8× intermediate magnification, 488 nm). Furthermore, we quantified the symmetry of the intracellular distribution of the nanoparticles. Student's *t*-test was used to test the effects of nanoconjugate treatment compared to the vehicle group (SAS JMP Inc, Cary, NC). Differences were considered significant if $p < 0.05$.

Author contributions

YBS: Conceptualization, funding acquisition, experimental design, performed experiments, analyzed data, provided super-

vision, wrote the first draft of the manuscript, reviewed and edited the manuscript. ESS: Experimental design, performed experiments, analyzed data, wrote the first draft of the manuscript, reviewed and edited the manuscript. EKC: Performed experiments, analyzed data, reviewed and edited the manuscript. KP: Performed experiments, analyzed data, reviewed and edited the manuscript. MA: Performed experiments, analyzed data, reviewed and edited the manuscript. EKL: Analyzed data, reviewed and edited the manuscript. JN: Analyzed data, reviewed and edited the manuscript. RML: Funding acquisition, provided supervision, reviewed and edited the manuscript.

Conflicts of interest

There are no conflicts to declare.

Data availability

The data that support the findings of this study will be made available from the corresponding author, upon reasonable request, starting 1 year after the online publication due to patenting process.

Supplementary information is available. Supplementary Movie: Super-resolution confocal image showing the intracellular distribution of glucose carbon dot-fluorescein conjugates in neurons.

Supplementary Fig. 1: Glial colocalization of glucose carbon dot-fluorescein conjugates in the cervical spinal cord following intravenous delivery.

Supplementary Fig. 2: Super-resolution confocal image showing the intracellular distribution of glucose carbon dot-fluorescein conjugates in neurons.

Supplementary Fig. 3: Photoluminescence spectra of glucose carbon dot(GluCD)-fluorescein and GluCD.

Supplementary Fig. 4A: *In vivo* systemic toxicity assessment of glucose carbon dots. See DOI: https://doi.org/10.1039/d5nr02670a.

References

1 R. H. Muller and C. M. Keck, *J. Biotechnol.*, 2004, **113**, 151–170.
2 W. M. Pardridge, *J. Cereb. Blood Flow Metab.*, 2012, **32**, 1959–1972.
3 M. M. Patel and B. M. Patel, *CNS Drugs*, 2017, **31**, 109–133.
4 W. M. Pardridge, *NeuroRx*, 2005, **2**, 3–14.
5 W. M. Pardridge, *Drug Discovery Today*, 2007, **12**, 54–61.
6 H. Liu, K. Dong, W. Zhang, S. G. Summerfield and G. C. Terstappen, *Drug Discovery Today*, 2018, **23**, 1357–1372.
7 D. Luptáková, T. Vallianatou, A. Nilsson, R. Shariatgorji, M. Hammarlund-Udenaes, I. Loryan and P. E. Andrén, *Mol. Psychiatry*, 2021, **26**, 7732–7745.
8 C. E. Brown-Séquard, Philadelphia University of California Libraries, 1858.
9 F. W. Mott, *Proc. R. Soc. London*, 1892, **50**, 120–121.
10 W. T. Porter, *J. Physiol.*, 1895, **17**, 455–485.
11 N. B. Finnerup and C. Baastrup, *Curr. Pain Headache Rep.*, 2012, **16**, 207–216.
12 A. D. Mickle, S. M. Won, K. N. Noh, J. Yoon, K. W. Meacham, Y. Xue, L. A. McIlvried, B. A. Copits, V. K. Samineni, K. E. Crawford, D. H. Kim, P. Srivastava, B. H. Kim, S. Min, Y. Shiuan, Y. Yun, M. A. Payne, J. Zhang, H. Jang, Y. Li, H. H. Lai, Y. Huang, S. I. Park, R. W. t. Gereau and J. A. Rogers, *Nature*, 2019, **565**, 361–365.
13 Z. Wang, A. Romanski, V. Mehra, Y. Wang, M. Brannigan, B. C. Campbell, G. A. Petsko, P. Tsoulfas and M. G. Blackmore, *eLife*, 2022, **11**, e76254.
14 A. C. Waddimba, N. B. Jain, K. Stolzmann, D. R. Gagnon, J. F. Burgess Jr., L. E. Kazis and E. Garshick, *Arch. Phys. Med. Rehabil.*, 2009, **90**, 193–200.
15 M. E. van den Berg, J. M. Castellote, J. de Pedro-Cuesta and I. Mahillo-Fernandez, *J. Neurotrauma*, 2010, **27**, 1517–1528.
16 M. J. Fishburn, R. J. Marino and J. F. Ditunno Jr., *Arch. Phys. Med. Rehabil.*, 1990, **71**, 197–200.
17 J. E. Riggs, Z. Guo, D. L. Carroll and Y.-P. Sun, *J. Am. Chem. Soc.*, 2000, **122**, 5879–5880.
18 Y.-P. Sun, B. Zhou, Y. Lin, W. Wang, K. A. S. Fernando, P. Pathak, M. J. Meziani, B. A. Harruff, X. Wang, H. Wang, P. G. Luo, H. Yang, M. E. Kose, B. Chen, L. M. Veca and S.-Y. Xie, *J. Am. Chem. Soc.*, 2006, **128**, 7756–7757.
19 X. Xu, R. Ray, Y. Gu, H. J. Ploehn, L. Gearheart, K. Raker and W. A. Scrivens, *J. Am. Chem. Soc.*, 2004, **126**, 12736–12737.
20 E. S. Seven, E. Kirbas Cilingir, M. Bartoli, Y. Zhou, R. Sampson, W. Shi, Z. Peng, R. Ram Pandey, C. C. Chusuei, A. Tagliaferro, S. Vanni, R. M. Graham, Y. B. Seven and R. M. Leblanc, *J. Colloid Interface Sci.*, 2023, **630**, 306–321.
21 S. D. Hettiarachchi, R. M. Graham, K. J. Mintz, Y. Zhou, S. Vanni, Z. Peng and R. M. Leblanc, *Nanoscale*, 2019, **11**, 6192–6205.
22 S. D. Hettiarachchi, E. Kirbas Cilingir, H. Maklouf, E. S. Seven, S. Paudyal, S. Vanni, R. M. Graham and R. M. Leblanc, *Nanoscale*, 2021, **13**, 5507–5518.
23 P. Y. Liyanage, S. D. Hettiarachchi, Y. Zhou, A. Ouhtit, E. S. Seven, C. Y. Oztan, E. Celik and R. M. Leblanc, *Biochim. Biophys. Acta, Rev. Cancer*, 2019, **1871**, 419–433.
24 E. S. Seven, S. K. Sharma, D. Meziane, Y. Zhou, K. J. Mintz, R. R. Pandey, C. C. Chusuei and R. M. Leblanc, *Langmuir*, 2019, **35**, 6708–6718.

25 E. S. Seven, Y. B. Seven, Y. Zhou, S. Poudel-Sharma, J. J. Diaz-Rucco, E. Kirbas Cilingir, G. S. Mitchell, J. D. Van Dyken and R. M. Leblanc, *Nanoscale Adv.*, 2021, **3**, 3942–3953.

26 W. A. Banks, A. J. Kastin and E. G. Gutierrez, *Neurosci. Lett.*, 1994, **179**, 53–56.

27 W. Pan, W. A. Banks and A. J. Kastin, *J. Neuroimmunol.*, 1997, **76**, 105–111.

28 V. Bartanusz, D. Jezova, B. Alajajian and M. Digicaylioglu, *Ann. Neurol.*, 2011, **70**, 194–206.

29 J. L. Shirley, Y. P. de Jong, C. Terhorst and R. W. Herzog, *Mol. Ther.*, 2020, **28**, 709–722.

30 H. M. Gebril, A. Aryasomayajula, M. R. N. de Lima, K. E. Uhrich and P. V. Moghe, *Transl. Neurodegener.*, 2024, **13**, 2.

31 K. Emmerich, D. T. White, S. P. Kambhampati, G. L. Casado, T.-M. Fu, Z. Chunawala, A. Sahoo, S. Nimmagadda, N. Krishnan, M. T. Saxena, S. L. Walker, E. Betzig, R. M. Kannan and J. S. Mumm, *Commun. Biol.*, 2023, **6**, 534.

32 G. Zhong, H. Long, T. Zhou, Y. Liu, J. Zhao, J. Han, X. Yang, Y. Yu, F. Chen and S. Shi, *Biomaterials*, 2022, **288**, 121690.

33 M. Battaglini, A. Marino, M. Montorsi, A. Carmignani, M. C. Ceccarelli and G. Ciofani, *Adv. Healthc. Mater.*, 2024, **13**, e2304180.

34 L. C. Schmued and J. H. Fallon, *Brain Res.*, 1986, **377**, 147–154.

35 H. T. Chang, H. Kuo, J. A. Whittaker and N. G. Cooper, *J. Neurosci. Methods*, 1990, **35**, 31–37.

36 L. Novikova, L. Novikov and J. O. Kellerth, *J. Neurosci. Methods*, 1997, **74**, 9–15.

37 S. E. Mondello, S. C. Jefferson, W. A. O'Steen and D. R. Howland, *J. Neurosci. Methods*, 2016, **270**, 85–91.

38 M. Bentivoglio, H. G. Kuypers, C. E. Catsman-Berrevoets, H. Loewe and O. Dann, *Neurosci. Lett.*, 1980, **18**, 25–30.

39 A. Rosina, *Neurosci. Lett.*, 1982, **33**, 217–221.

40 F. Condé, *J. Neurosci. Methods*, 1987, **21**, 31–43.

41 F. J. Richmond, R. Gladdy, J. L. Creasy, S. Kitamura, E. Smits and D. B. Thomson, *J. Neurosci. Methods*, 1994, **53**, 35–46.

42 C. B. Mantilla, W. Z. Zhan and G. C. Sieck, *J. Neurosci. Methods*, 2009, **182**, 244–249.

43 Y. B. Seven, A. K. Simon, E. Sajjadi, A. Zwick, I. Satriotomo and G. S. Mitchell, *Exp. Neurol.*, 2020, **323**, 113067.

44 C. R. Gerfen, D. D. O'Leary and W. M. Cowan, *Exp. Brain Res.*, 1982, **48**, 443–448.

45 P. J. Harrison, H. Hultborn, E. Jankowska, R. Katz, B. Storai and D. Zytnicki, *Neurosci. Lett.*, 1984, **45**, 15–19.

46 E. Jankowska, *Brain Res.*, 1985, **341**, 403–408.

47 H. G. Goshgarian and J. L. Buttry, *J. Neurosci. Methods*, 2014, **222**, 156–164.

48 J. P. Card, L. Rinaman, J. S. Schwaber, R. R. Miselis, M. E. Whealy, A. K. Robbins and L. W. Enquist, *J. Neurosci.*, 1990, **10**, 1974–1994.

49 S. Chen, M. Yang, R. R. Miselis and G. Aston-Jones, *Brain Res.*, 1999, **838**, 171–183.

50 Z. Boldogköi, A. Reichart, I. E. Tóth, A. Sik, F. Erdélyi, I. Medveczky, C. Llorens-Cortes, M. Palkovits and Z. Lenkei, *Brain Res Mol Brain Res*, 2002, **109**, 105–118.

51 A. E. Granstedt, M. L. Szpara, B. Kuhn, S. S. Wang and L. W. Enquist, *PLoS One*, 2009, **4**, e6923.

52 A. E. Granstedt, B. Kuhn, S.-H. Wang and L. W. Enquist, *Cold Spring Harb. Protoc.*, 2010, **2010**, pdb.prot5410.

53 J. P. Card and L. W. Enquist, *Curr. Protoc. Neurosci.*, 2014, **68**, 1.5.1–1.5.39.

54 J. N. Sleigh, G. A. Weir and G. Schiavo, *BMC Res. Notes*, 2016, **9**, 82.

55 Y. B. Seven, R. R. Perim, O. R. Hobson, A. K. Simon, A. Tadjalli and G. S. Mitchell, *J. Physiol.*, 2018, **596**, 1501–1512.

56 Y. B. Seven, N. L. Nichols, M. N. Kelly, O. R. Hobson, I. Satriotomo and G. S. Mitchell, *Exp. Neurol.*, 2018, **299**, 148–156.

57 L. L. Allen, N. L. Nichols, Z. A. Asa, A. T. Emery, M. C. Ciesla, J. V. Santiago, A. E. Holland, G. S. Mitchell and E. J. Gonzalez-Rothi, *Exp. Neurol.*, 2021, **346**, 113832.

58 M. C. Ciesla, Y. B. Seven, L. L. Allen, K. N. Smith, Z. A. Asa, A. K. Simon, A. E. Holland, J. V. Santiago, K. Stefan, A. Ross, E. J. Gonzalez-Rothi and G. S. Mitchell, *Exp. Neurol.*, 2021, **338**, 113609.

59 M. C. Ciesla, Y. B. Seven, L. L. Allen, K. N. Smith, E. J. Gonzalez-Rothi and G. S. Mitchell, *Exp. Neurol.*, 2022, **347**, 113903.

60 Y. B. Seven, L. L. Allen, M. C. Ciesla, K. N. Smith, A. Zwick, A. K. Simon, A. E. Holland, J. V. Santiago, K. Stefan, A. Ross, E. J. Gonzalez-Rothi and G. S. Mitchell, *Neuroscience*, 2022, **506**, 38–50.

61 F. J. Golder, D. D. Fuller, M. R. Lovett-Barr, S. Vinit, D. K. Resnick and G. S. Mitchell, *Exp. Neurol.*, 2011, **231**, 97–103.

62 S. Alvarez-Argote, H. M. Gransee, J. C. Mora, J. M. Stowe, A. J. Jorgenson, G. C. Sieck and C. B. Mantilla, *J. Neurotrauma*, 2016, **33**, 500–509.

63 S. Rana, G. C. Sieck and C. B. Mantilla, *J. Neurophysiol.*, 2017, **117**, 545–555.

64 P. M. Warren, C. Campanaro, F. J. Jacono and W. J. Alilain, *Exp. Neurol.*, 2018, **306**, 122–131.